International Journal of the Physical Sciences Vol. 6(6), pp. 1293-1305, 18 March, 2011
Available online at http://www.academicjournals.org/IJPS
DOI: 10.5897/IJPS11.065
ISSN 1992 - 1950 ©2011 Academic Journals

Full Length Research Paper

Development of a composite autofocus method for tissue slides using a line scan CCD camera

Jiun-Hung Yu*, Ting-Hsuan Chen, Chih-Wei Liao, Yen-Chung Chen and Fang-Jung Shiou

Department of Mechanical Engineering, National Taiwan University of Science and Technology, Taipei 10607, Taiwan, ROC, Taiwan.

Accepted 14 March, 2011

This study describes the application of a composite autofocus method, which combines full-trip auto focusing (AF) technology with extended depth of field (EDOF) technology to examine tissue slides, using a line scan CCD camera. We investigated several criteria that serve as appropriate sharpness evaluation methods, for histological images. Examples of such methods include the use of an edge detection filter for the spatial domain and energy computation for the frequency domain. A tissue slice, taken for histological examination generally has a certain thickness, but due to the limitations in the depth of field (DOF) of the objective lens, it is not possible to ensure that the tissue section stays within the DOF of the objective lens, during the image acquisition process. Factors such as the thickness of the tissue slice, defects in the production process for the tissue slide and mechanical error impact the quality of the final slide. Our study focuses on the motion of the line scan CCD camera along the Z-axis, during the image acquisition process. Motion along the Z-axis allows for instant AF, during image acquisition. A guide curve, for Z/X-axis shift to the other layers, along with our proposals, can yield sharper images.

Key words: Autofocusing (AF), tissue slide, microscopy, histologic, line scan.

INTRODUCTION

An automatic microscope is used during tissue slice examination, to increase the reliability of any pathological interpretation and to ensure the repeatability of AF. These are issues that may affect the processing and analysis of an image by a computer program. This study proposes an examination of a few of the issues, with respect to AF in histological microscopy.

The study draws on the experiences of earlier studies (Firestone et al., 1991; Groen et al., 1985; Harms and Aus, 1984; Mea et al., 2005; Strang, 1999; He et al., 2003) for a discussion of some of the more successful methods of AF, especially its application to histological microscopic research, in order to propose a more effective solution.

When a tissue slice is cut from the human body, animals, or plants, the slice goes through a process (Eguíluz et al., 2006) to produce a tissue slide. Even if the tissue slice is cut with a precision instrument (microtome), there are still quality issues with the precision-cut tissue slice.

Figure 1 shows a broad outline of tissue slide production. Each step can cause uneven slice thickness. Since problems with cell biology exist in three-dimensional space, there is no way to avoid focusing on multiple layers of the tissue slice. In this study, the use of line scan camera for image acquisition requires accurate horizontal leveling, during relative motion of the camera. If this is not the case, the continuous motion during image acquisition can easily cause the image to move outside the DOF. Due to the limitations of the DOF, when one layer comes into focus, the other layers will appear blurred (Pieper and Korpel, 1983; Dowski and Cathey, 1995; Zhang and Blum, 1999; Li et al., 1994; Forster et al., 2004). Consequently, if an important part of the sample occupies multiple layers, it is impossible to obtain a sharp image of that part in its entirety, by focusing only on one layer.

To overcome problems with tissue surface irregularity, horizontal leveling accuracy and multilayer focusing, we will discuss several AF algorithms and assess their suitability for histological microscopy. The algorithms will

*Corresponding author. E-mail: D9703208@mail.ntust.edu.tw. Tel: +886-2-27333141 ext. 7348. Fax: +886-2-27376460.

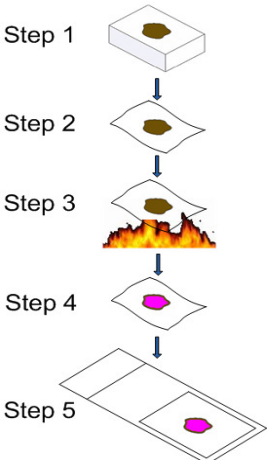

Figure 1. Production process for a tissue slice.

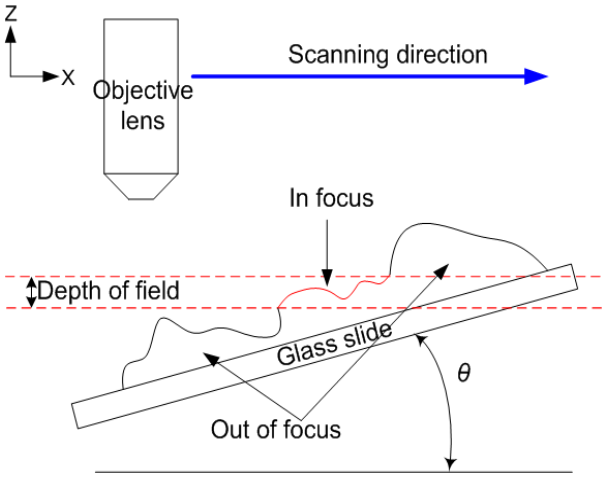

Figure 2. Out of focus scanning process.

be used to construct and test a highly efficient, composite AF program. Finally, experimental results will show that the methods examined in this study can provide solutions to the problems previously discussed. This study also proposes a process for obtaining sharper images, which has much simpler AF steps than previous studies.
The process for production of a tissue slide follows these steps:

Step 1: Embed the tissue in melting wax to form a tissue microarray.
Step 2: Use microtome to section off slices ranging from 2 to 5 µm in thickness.
Step 3: Dry in a vacuum.
Step 4: Stain the tissue slice.
Step 5: Mount the tissue slice on a standard slide.

In this process, the quality of the wax block and microtome will affect the quality of the tissue slice. Bubbles may also form during mounting of the tissue slice on the slide. These factors can cause irregularities on the surface of the tissue slice. As a result, the image within the scanning range does not fit within the DOF. Any error in horizontal leveling of the moving stage will also change the distance between the objective lens and the surface of the tissue, causing parts of the sample to be outside the DOF. Figure 2 shows the focus diagram for an objective lens and tissue slide. The red dotted line shows DOF. Any image that exceeds this range will result in an image that is only partly in focus.

MATERIALS AND METHODS

Experimental details of the auto-focusing system

The passive auto-focusing system consists of a microscopy unit (MS1, VS), attached to both an area scan CCD camera and a line scan CCD camera. The area scan camera carries out the auto-focusing at each measurement point, determined by a preview camera. The line scan camera captures the full trip-scanning image in focus. Image digitization is performed by an image acquisition card (PCI-1429, NI), which also contains a digital signal processor and a graphics processor, for high-speed image processing and display.

The distance between the tissue slide and the microscope's objective lens (40×, NA = 0.6, Nikon) is controlled by a motion control card (PCI-7344, NI). This unit controls the voice coil motor (XRV76-20, linear scale: 0.1 µm, Akribis), which drives the stage in the Z-axis direction. The motion card also controls the dual-axis motion stage. In the x-axis direction, the motion stage uses a voice coil motor (LAS55-100-5, linear scale: 0.1 µm, SMAC), while movement in the Y-axis direction uses a micro stepper motor with a 0.1 µm linear scale. The CPU is an Intel Core 2 Dou E6750 2.66 GHz; the RAM was DDR2 2GB, and the programming language is LabVIEW 8.5. Figure 3 shows the auto-focusing and scanning systems.

Methods

As described previously, this study used three image acquisition systems and a three-axis motion stage. The area scan camera was used for passive AF decisions, at various measurement points. The line scan camera then positioned itself in accordance with the focusing information at these measurement points to capture a sharp histological image. The preview camera was used to capture the tissue slide image in its entirety in order to create the circled selection of the scanning area.

Since the line scan camera needs to maintain a constant velocity relative to the imaging object in order to record the image correctly, it must carry out AF within the same field of view (FOV). The line scan camera must continue its motion, back and forth, along the x-axis, while staying within the same FOV, in order to capture the same image. Only then can the sharpness of the image be analyzed.

For this mode, image acquisition is not continuous and is time consuming. In this study, a beam splitter was connected to the area scan camera and the line scan camera, so that both cameras could share the same objective lens. The two cameras formed an imaging center that served as the co-axis for the camera motion. This increased the speed of image capture, within the same FOV, and

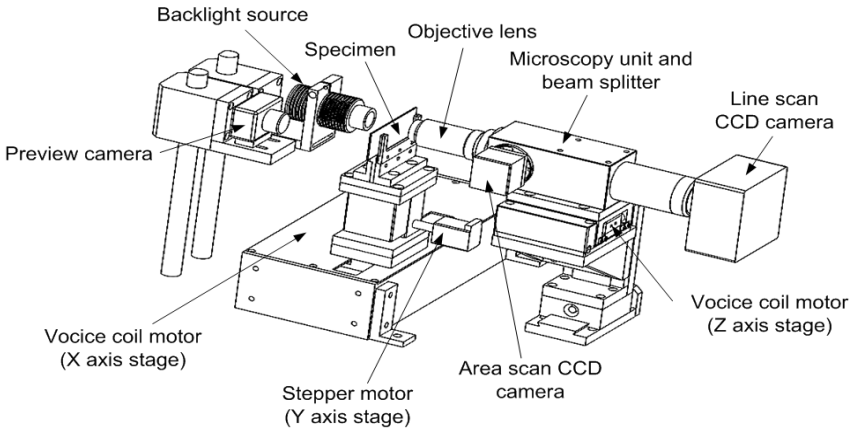

Figure 3. Diagram of experimental equipment.

saved the time that would be spent having the motion stage repeatedly moving back and forth.

The full-trip AF method relies on the area scan camera being able to carry out AF at several measurement points along the same image acquisition trip. A second order curve can then be synthesized, using the focusing information that was gathered. As the line scan camera captures images at a fairly constant velocity, the z-axis distance between the objective lens and tissue slide continuously changes, in accordance with the focusing information provided by the second-order curve. As a result, a tissue section that occupies the same layer within the range of the full trip can remain within the DOF.

The EDOF technique (Dowski and Cathey, 1995; Prabhat et al., 2006) was then used to shift the focusing guide curve, in order to capture images from various layers. These captured multi-images were then merged together. The following are the AF steps in this study:

Step 1: Use the preview camera to create a circled selection of the scanning areas on the screen.
Step 2: Perform scanned area image binarization (National Instruments Corporation, 2000), to determine the number of measurement points.
Step 3: Use the area scan to AF on each measurement point and record the height of each measurement point, on the z-axis.
Step 4: Calculate the acceleration and deceleration at each measurement point on the z-axis.
Step 5: Complete a guide curve of the full-trip AF.
Step 6: Shift the guide curve, capture images at various layers.
Step 7: Complete the fusion of multilayer images.

Operations before AF

Transformation of vision/ motion coordinates: Before scanning the tissue slide, the system first must know the scanning range and the AF measurement points (center of the measuring area). This study used a low magnification preview camera to capture an image of a calibration scale, which covered the entire area of slide. The information from this image first underwent magnification calibration and then correction of motion coordinates. Its low-magnification imaging information was then used to determine both the AF position (area scan camera) and scanning (line scan camera) range. The entire system used three coordinate systems: The globe coordinates G (x,y), for the motion control; the machine coordinates M(x,y), for the scanning system (Cam1); the Image coordinates $C_2(x,y)$, for the preview camera (Cam2). In Figure 4, (a) shows the image of the calibration scale, captured by Cam1. The globe position of Cam1 is in accordance with the image coordinates C_1 (x_c,y_c) using Equations (1) to transform to G (j,k). This point is defined as the orgin M (0,0) of scanning coordinates. Figure 4 (b) shows the relative positions of the various cameras. M (p,q) is the position of Cam2, it covers the entire area of the slide. The transformation formulas are shown in Equations (2), where the AF and scanning systems were used as co-axis (Kuo et al., 2008; Nian and Trang, 2005).

The calibration step are:

1. Capture an image C_1 of the calibration scale using Cam1.
2. Measured the center position $C_1(x_c,y_c)$ of the red target circle in image C_1.
3. According to the distance between $C_1(0,0)$ and $C_1(x_c,y_c)$, move cam1 to G (j,k), which is defined as the origin M(0,0) of machine coordinate.
4. Move the calibration scale to the FOV of Cam2, using XY stage. The posion could be covering entire area of slide, and define this position as M(p,q).
5. The center of the red target circle in the FOV of Cam2 was defined as $C_2(0,0)$.
6. Calibrated the magnification between Cam1and Cam2.
7. Scan the tissue slide, selected any ROI in FOV of Cam2 (start point x_s,y_s and retangle size x_r,y_r).

$$M(0,0)_{pulse} \equiv G(j,k)_{pulse} \equiv \begin{bmatrix} c_x & 0 \\ 0 & c_y \end{bmatrix}^{-1}_{pulse/mm} \left(\begin{bmatrix} b_x & 0 \\ 0 & b_y \end{bmatrix}_{mm/pixel} \begin{bmatrix} x_c \\ y_c \end{bmatrix}_{pixel} \right) \quad (1)$$

$$\begin{cases} \begin{bmatrix} S_x \\ S_y \end{bmatrix}_{pulse} = \begin{bmatrix} c_x & 0 \\ 0 & c_y \end{bmatrix}^{-1}_{pulse/mm} \left(\begin{bmatrix} a_x & 0 \\ 0 & a_y \end{bmatrix}_{mm/pixel} \begin{bmatrix} x_s \\ y_s \end{bmatrix}_{pixel} + \begin{bmatrix} c_x & 0 \\ 0 & c_y \end{bmatrix}_{mm/pulse} \begin{bmatrix} p \\ q \end{bmatrix}_{pulse} \right) \\ \begin{bmatrix} R_x \\ R_y \end{bmatrix}_{pixel} = \left(\begin{bmatrix} a_x & 0 \\ 0 & a_y \end{bmatrix}_{mm/pixel} \begin{bmatrix} b_x & 0 \\ 0 & b_y \end{bmatrix}^{-1}_{pixel/mm} \right)^T \begin{bmatrix} x_r \\ y_r \end{bmatrix}_{pixel} \end{cases} \quad (2)$$

S_x and S_y is the start positions of Cam1 (line scan); R_x and R_y are the size of the scanning rectangle; x_s and y_s are the point of top left of ROI rectangle; x_r and y_r are the size of ROI retangle; a is the correction value for the preview camera; p and q are the relative motion pulses between Cam1 and Cam2; c is the motion correction

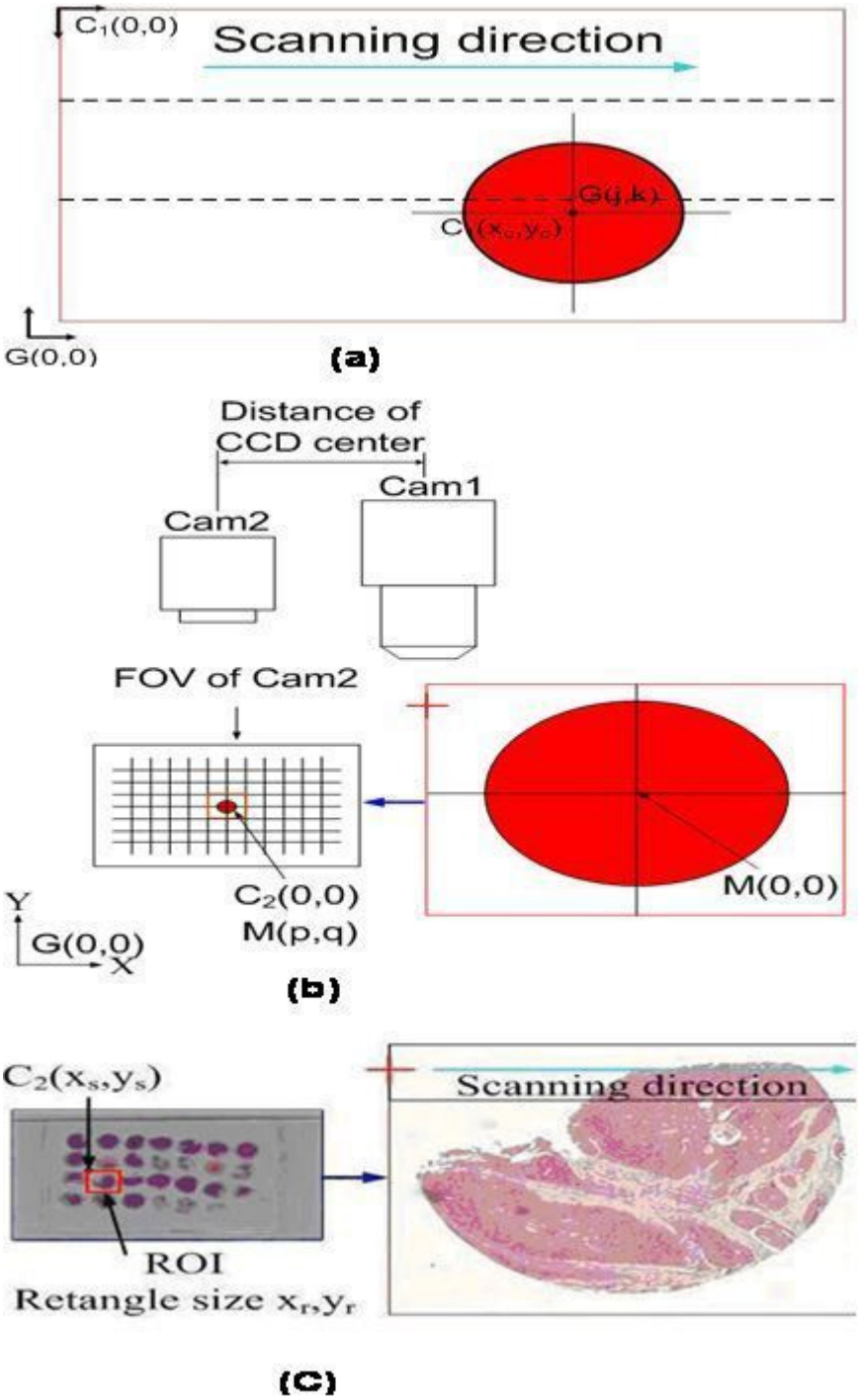

Figure 4. Diagram showing coordinate transformation (a) step 1 to 2, (b) step 3 to 6, and (c) step 7.

value, x_c and y_c are the center of the red circle of Cam1, and b is the correction value for Cam1.

Determination of measurement points

When focusing the camera on the tissue slide, this is often due to limitation of low image information within the focus range, so the AF is unable to perform any measurement on the image. We had to make judgment and decide the number of measuring point P_i within the scanning range, before AF. In Figure 5, the part that is colored pink is an irregular tissue slice, which is surrounded by transparent glass. In order to identify which part contains tissue, the image was processed, using binarization and morphology (National

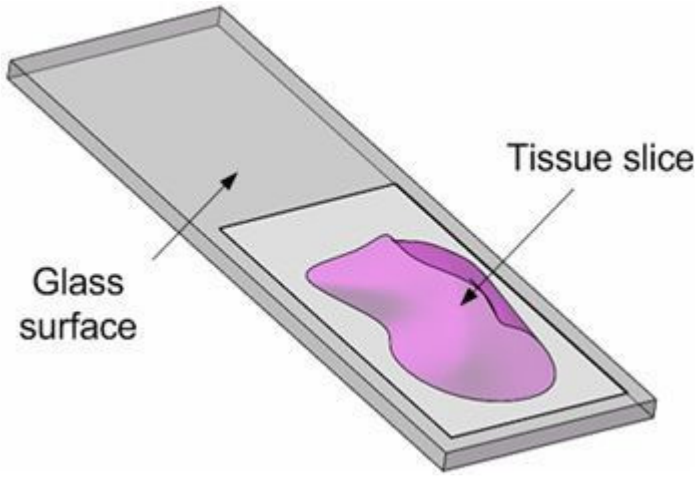

Figure 5. Diagram of tissue slide.

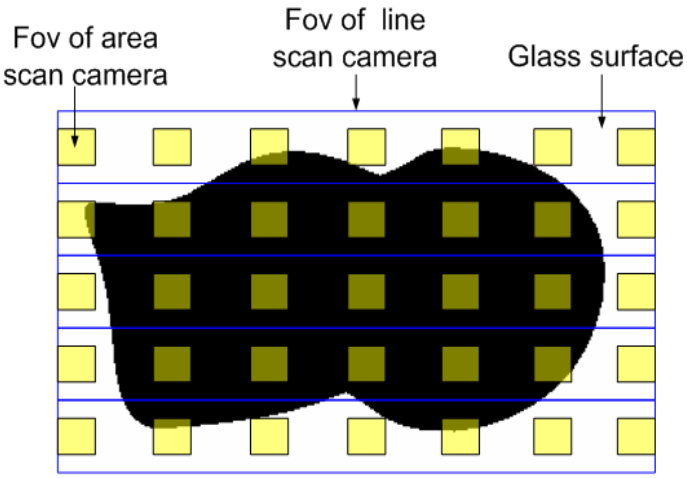

Figure 6. Diagram of binary image.

Instruments Corporation, 2000; Rafael and Woods, 2002) treatments. Figure 6 shows the tissue image after it has been subject to binarization. The long blue box contains images taken with the line scan camera moving along the x-axis.

The yellow box is the area scan camera's range of image capture, *MxN*. If the yellow box contains enough material, then it is defined as a measurement point. As shown in Equation (3), when the summarized value of the binarized image within the yellow box is greater than the established experience threshold value, it is defined as a measurement point, but if it is smaller than the experience threshold value, then that point is defined as the surface of the glass.

$$\sum I(x,y) = \begin{cases} \text{Mesuring point}, & \text{if} > T \\ \text{The surface of the glass}, & \text{if} < T \end{cases} \quad (3)$$

$x = 0 \sim M \quad y = 0 \sim N \quad \sum I(x,y)$ is the measurement area (yellow box).

AF for each measurement point

Focus measurement: A review of the literature regarding microscopic image focusing shows (Firestone et al., 1991; Groen et al., 1985; Harms and Aus, 1984) that AF measurement criteria can be divided into frequency domain-based algorithms, spatial domain-based algorithms, and statistically-based algorithms. Image contrast measurement estimates the focus quality by evaluating the image contrast, with reference to its gray level variance and derivatives. A typical example is the standard deviation (Mea et al., 2005). The characteristics of a tissue slice were assessed for its discrete cosine transform (DCT), within the frequency domain (Strang, 1999). The characteristics were also assessed using Laplacian, Sobel and Prewitt edge detector filters (National Instrument Corporation, 2007), based on AF measurement crieria. Table 1 show that the Laplacian edge detector filter displayed the largest standard deviation. The Laplacian edge detector filter was thus best suited to histological AF measurements, but as the image filtered by Laplacian transform as Figure 7(a) and (b), shows, the image exhibited excessive noise. This would probably cause noise

Table 1. Standard deviation of various edge detector filters.

Edge detect filter	Sobel	Laplacian	Prewitt
Mean value	35.83	31.62	34.55
Standard dev	32.33	54.31	30.85

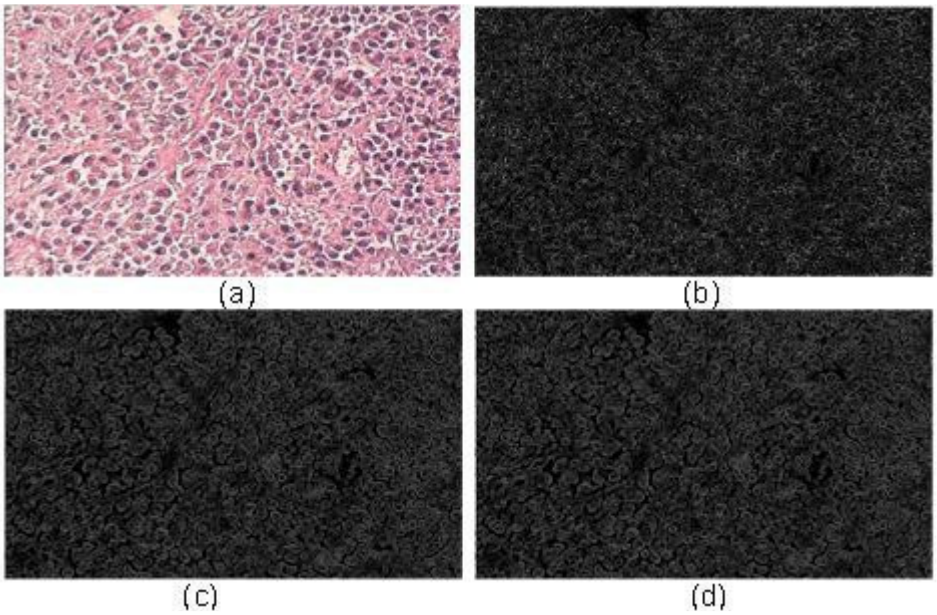

Figure 7. Image of a histological sample, (a) original image (b) Laplacian (c) Prewitt (d) Sobel.

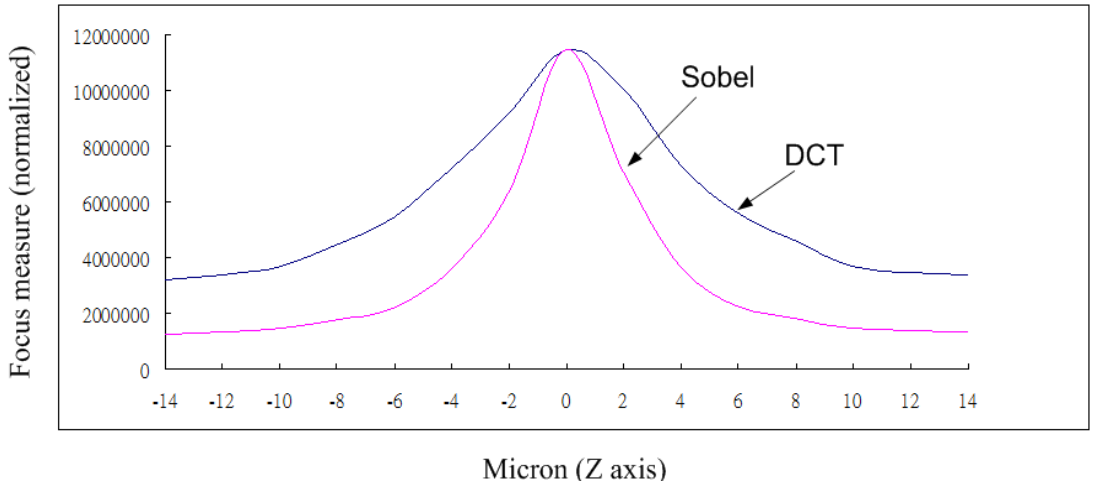

Figure 8. DCT and Sobel focus curve diagram.

interference, when making focusing judgments. Figures 7(c) and (d) show the images filtered by Sobel and Prewitt edge detectors. The quality of these two filters was very similar; but Sobel displayed a larger standard deviation, which represents the relative sharpness of the image at its border.

The Sobel edge detector filter had a better focusing effect on the histological image. This study used a Sobel edge detector filter as a focusing standard for focusing curve comparison with DCT, for the frequency domain. The result is shown in Figure 8. The focus curve obtained using a Sobel edge detector showed a normal distribution

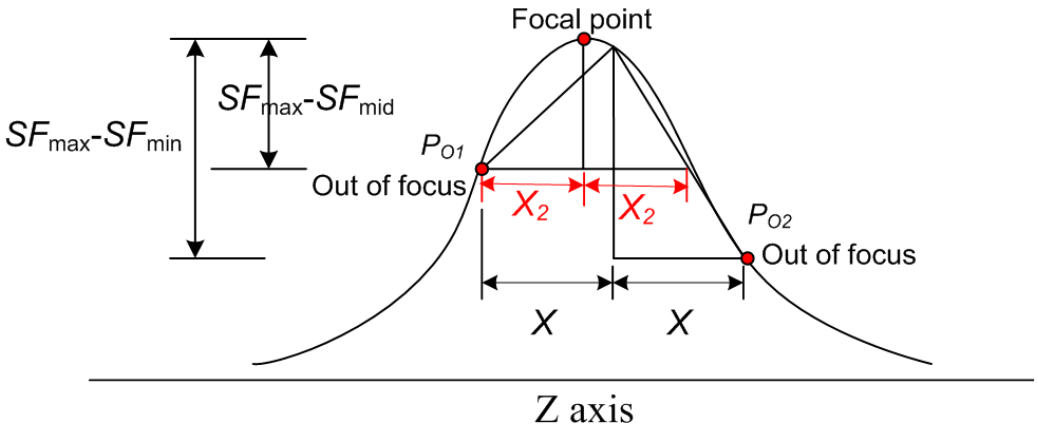

Figure 9. Focus search diagram.

pattern for its kurtosis. The focus curve obtained by DCT shows a distribution that is wider. With regard to the criteria of focus measurement, DCT exhibited greater stability than other methods.

Focus search algorithm: Resent focusing-related references have proposed numerous search methods. Hill climbing (He et al., 2003) is one such method that is widely used, because of its high accuracy. In this study, although the AF method used many measurement points, the focusing quality at the first measurement point was most important. Therefore, the hill climbing technique was used as the focus search method for the first measurement point. In order to save time searching for other measurement points, starting with P_2, the ratio of focus measurement value was used as the method to search for focal points, as shown in Equations (4) and (5).

As the DCT focus curve in Figure 8 shows, the focus measurement value rises and falls within a range of about ± 10 micron. The focus measurement value is also symmetrical on either side of the focal point. If the relative Z-axis distance between P_i and P_{i+1} is within ±10 micron, then the ratio method can be used to calculate the position of the focal point.

As shown in Figure 9, when the z-axis moves from P_i to P_{i+1}, it may pass out of the range of DOF until it reaches P_{O1} or P_{O2}. At that point, the z-axis stage can increase or decrease, by the amount of X_2 using the SF ratio relationship. The correct position of P_{i+1} can thus be obtained from Equations (4) and (5). The X must be within ±10 micron, which is the limitation of non flat section of focusing curve.

$$S = \frac{SF_{max} - SF_{mid}}{SF_{max} - SF_{min}} \tag{4}$$

$$X_2 = \frac{(1+S)X}{2} \tag{5}$$

where SF is the value of the sharpness function and X and X_2 depict the increment of motion.

Composite auto-focusing methods, using a line scan camera

Build guide curve using the relationship between x- axis and z- axis: Irregularities in the tissue slice could be due to an air gap, or inaccuracy with the microtome. The surfaces of these irregularities are generally a smooth arc, since the line scan camera needs to maintain a fairly constant velocity, relative to the imaging object, in order to record the image correctly.

During image acquisition, at a constant velocity, AF information, from P_i, from the area scan camera, was used to control acceleration and deceleration along the Z-axis, which depicted a sub-guide curve (S-shaped curve). Figure 10 shows the position, velocity, acceleration and time relational diagram, along the x axis and z axis. Constant velocity was maintained along the x-axis, between P_i and P_{i+1}. The time taken, to travel this distance, is T_1. The z-axis distance, between P_i and P_{i+1}, must be completely traversed within time T_1.

Figure 10 (b) shows z-axis movement to $(P_i+P_{i+1})/2$, at a constant acceleration, and then a deceleration towards P_{i+1}. Figures 10 (c) and (d) show the sub-guide curve for the x/z-axis. Equation (6) shows the acceleration and deceleration equations for the distance between each point, along the Z-axis.

$$t_{x_{i\sim(i+1)}} = t_{z_{i\sim\frac{i+(i+1)}{2}}} + t_{z_{\frac{i+(i+1)}{2}\sim(i+1)}}$$

$$\frac{x_{i+1} - x_i}{v_x} = \left(\frac{\left(z_{\frac{i+(i+1)}{2}} - z_i \right)}{\frac{dv_z}{dt}} \right)^{\frac{1}{2}} + \left(\frac{\left(z_{i+1} - z_{\frac{i+(i+1)}{2}} \right)}{\frac{dv_z}{dt}} \right)^{\frac{1}{2}}$$

$$\left(\frac{\left(z_{\frac{i+(i+1)}{2}} - z_i \right)}{\frac{dv_z}{dt}} \right)^{\frac{1}{2}} = \left(\frac{\left(z_{i+1} - z_{\frac{i+(i+1)}{2}} \right)}{\frac{dv_z}{dt}} \right)^{\frac{1}{2}}$$

$$a_z = \pm \frac{2v_x^{\,2}\left(z_{i+1} - z_i\right)}{\left(x_{i+1} - x_i\right)^2} \tag{6}$$

There are (n-1) sub-guide curves in P_i. On the surface of tissue slide, the interval between each P_i was a decision by the human,

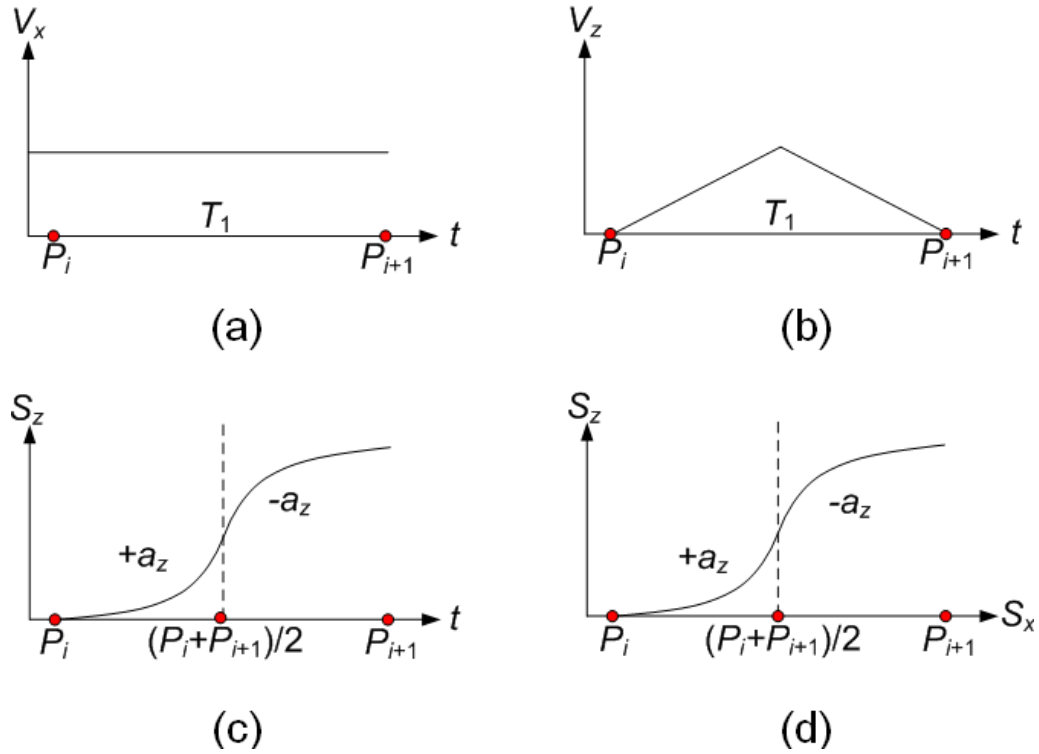

Figure 10. Velocity, acceleration, time along the Z/X-axis. V_x is velocity along the x-axis, V_z is velocity along the z-axis, S_x is x-axis distance and S_z is z-axis distance.

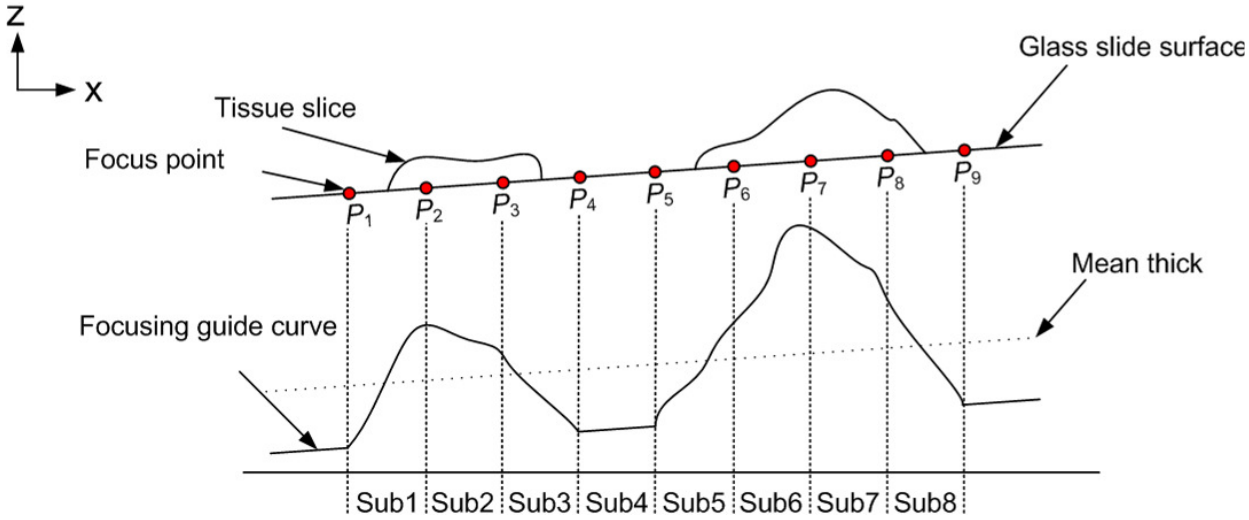

Figure 11. Diagram of focus guide curve.

smaller interval could acquire more detail of the curves; lager interval could save the consuming. These (n-1) curves will rise and fall, along the surface of the tissue section. Figure 11 shows eight complete focus sub-guide curves, where P_1, P_4, P_5 and P_9 were judged as the surface locations of the glass. In order to save overall focusing time, the AF was not used at these point locations. The average height of the full-trip was used as the benchmark for the Z axis positions of these point locations.

Extended DOF histological microscopic imaging: Tissue slice thickness ranges from 2 to 5 µm. Full-trip AF can smooth the irregularities of a surface of tissue slice, but each cell, within the slice, has a thickness. When Extended Depth-of-Field Microscope Imaging was used, the complete guide curve, previously mentioned was repeated for various layers, to capture histological images. Figure 12 shows the guide curve shifted by N layers, to accommodate the slice thickness. Image acquisition, using the

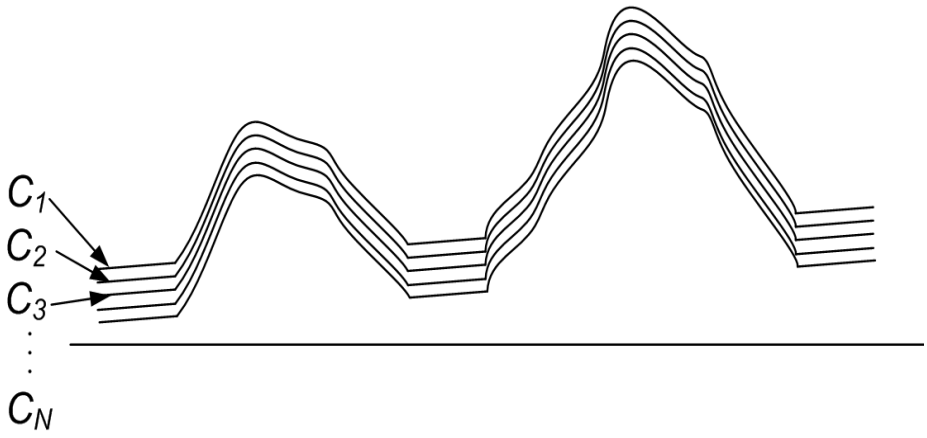

Figure 12. Diagram of extended depth-of-field curve.

Guide Curve for various layers forms the extended DOF image, when a fusion map is created (Pieper and Korpel, 1983; Tympel, 1996; Zhang and Blum, 1999; Li et al., 1994; Forster et al., 2004). The image of a section is captured, using the guide curves, for *N* layers, as $I_C^1(x,y)$, $I_C^2(x,y)$ . . . , $I_C^N(x,y)$. The component focus, measured for each of these images at location (x,y), is $R_C^n(x,y)$, *n* = 1, 2 . . . , *N*. The fusion map is then defined by Equation (7) (Dowski and Cathey, 1995), which is an index function, with integer values ranging from 1 to *N*. The composite image, resulting from image fusion is given by Equation (8).

$$M(x,y) = \arg\max_n \left| R_C^n(x,y) \right| \quad n = 1,2,...N \tag{7}$$

$$I_C(x,y) = \bigcup_{n=M(x,y)} \{ I_C^n(x,y) \} \tag{8}$$

The measurement of component focus has been the subject of repeated developments, such as pixel-based image fusion (Pieper and Korpel, 1983), the neighborhood-based image fusion (Tympel, 1996) and the multi-resolution-based image fusion (Li et al., 1994; Forster et al., 2004). In this paper, the component focus, $R_C^n(x,y)$, is computed using a neighborhood-based image fusion method (Tympel,1996). It is computed based on a set of neighboring pixels, instead of individual pixels, as in the pixel-based schemes. The first type of neighborhood-based image fusion uses differential or gradient operations to process the images and characterize their focus measurement. Using a 3×3 differential operator, as in function (9) (Pieper and Korpel, 1983), or a 5×5 differential operator, as in function (10), each I_C^n is convolved to generate the component focus measurement:

$$R_C^n(x,y) = I_C^n(x,y) * \begin{bmatrix} -1 & 1 & 1 \\ -1 & 0 & 1 \\ -1 & -1 & 1 \end{bmatrix} \tag{9}$$

$$R_C^n(x,y) = I_C^n(x,y) * \begin{bmatrix} -1 & 1 & 1 & 1 & 1 \\ -1 & -2 & 2 & 2 & 1 \\ -1 & -2 & 1 & 2 & 1 \\ -1 & -2 & -2 & 2 & 1 \\ -1 & -1 & -1 & -1 & 1 \end{bmatrix} \tag{10}$$

The second type of neighborhood-based schemes considers some form of image variance in the neighborhood of every pixel, when the optical section images are fused. One algorithm uses the regional coefficient of variance, of a 5×5 area (Tympel, 1996). The component focus measurement in this case is defined as the square of the coefficient of variance based on the values of the pixels in the area. It is computed by

$$R_C^n(x,y) = \frac{\sum_{i=-2}^{2}\sum_{j=-2}^{2} \left(I_C^n(x+i,y+j) - \bar{I}_C^n(x,y) \right)^2}{25} \tag{11}$$

where

$$\bar{I}_C^n(x,y) = \frac{\sum_{i=-2}^{2}\sum_{j=-2}^{2} I_C^n(x+i,y+j)}{25}$$

RESULTS

Figure 13 shows a specimen human tissue slice. The methods developed in this study were used to select the area to be scanned, as well as to auto-detect the number of measurement points, for AF. Figure 14 shows the circled selections of the scanned area of the tissue slice and the measurement points. Table 2 shows the acceleration and deceleration, at various intervals along the Z-axis, the position of various measurement points and the number of scanned layers. Full-trip AF was used to smooth the irregularity of the surface of the tissue slice, EDOF addressed focusing issues related to the fact that a cell exists in three-dimensional space. Figure 15 shows the results, using the composite AF method, in which different component focus measurements, $R_C^n(x,y)$, are fused, to create multilayer images. Finally, among these methods, the variance has the best performance.

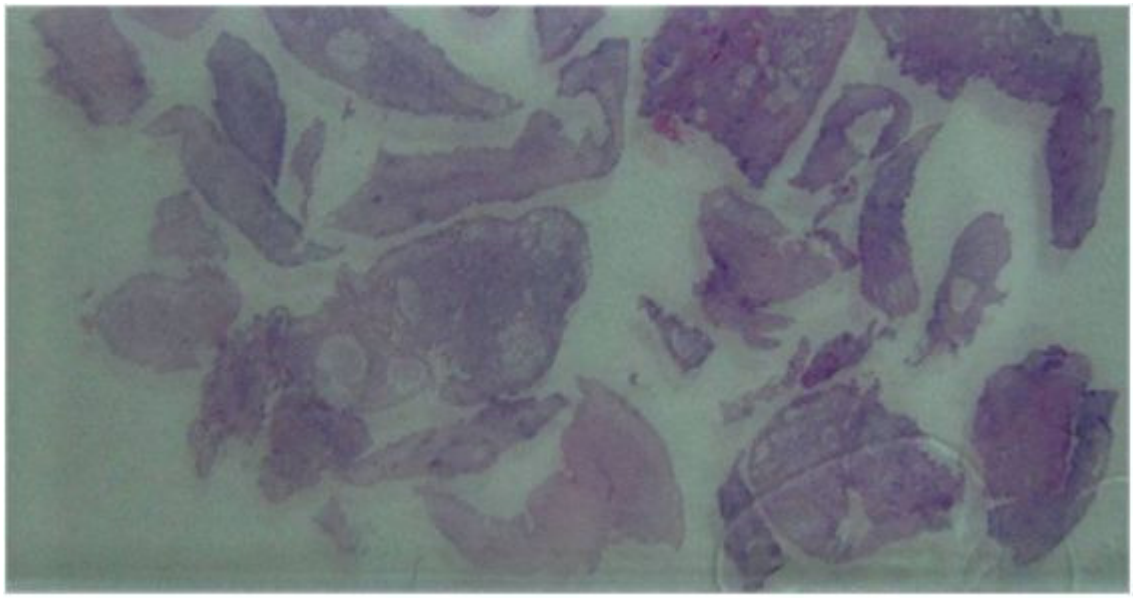

Figure 13. Specimen of a human tissue slice.

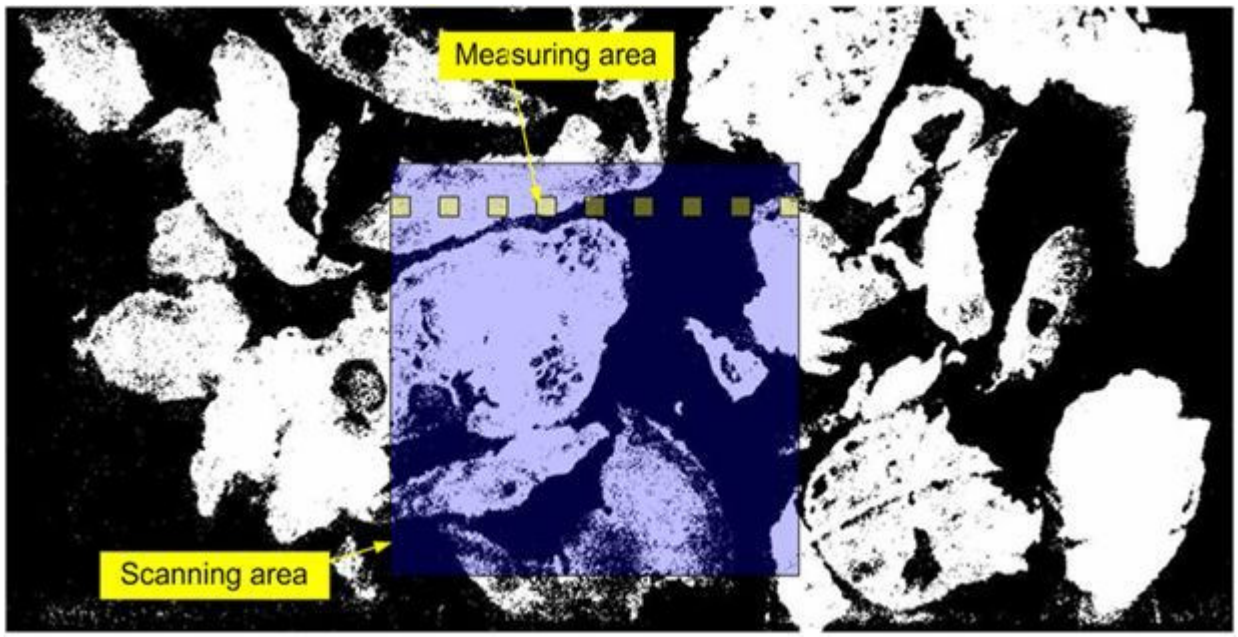

Figure 14. Circled selection of scanning areas and definition of measuring points (the center of the measuring areas).

Table 2. Results data of composite AF methods.

Specimen	P_1	P_2	P_3	P_4	P_5	P_6	P_7	P_8	P_9
Z axis position (μm)	325.2	327.8	327.2	326.9	328.1	327.6	327.7	327.8	330.2
Number of scanning layer	5 layers, interval of each layer was 2 μm								
Intervals	P_1- P_2	P_2- P_3	P_3 -P_4	P_4 -P_5	P_5 -P_6	P_6 -P_7	P_7 -P_8	P_8- P_9	
Z axis acceleration (μm/s^2)	±5.2	±1.2	±0.6	±2.4	±1	-	-	±4.8	

*P_6, P_7, P_8 was the surface of the glass.

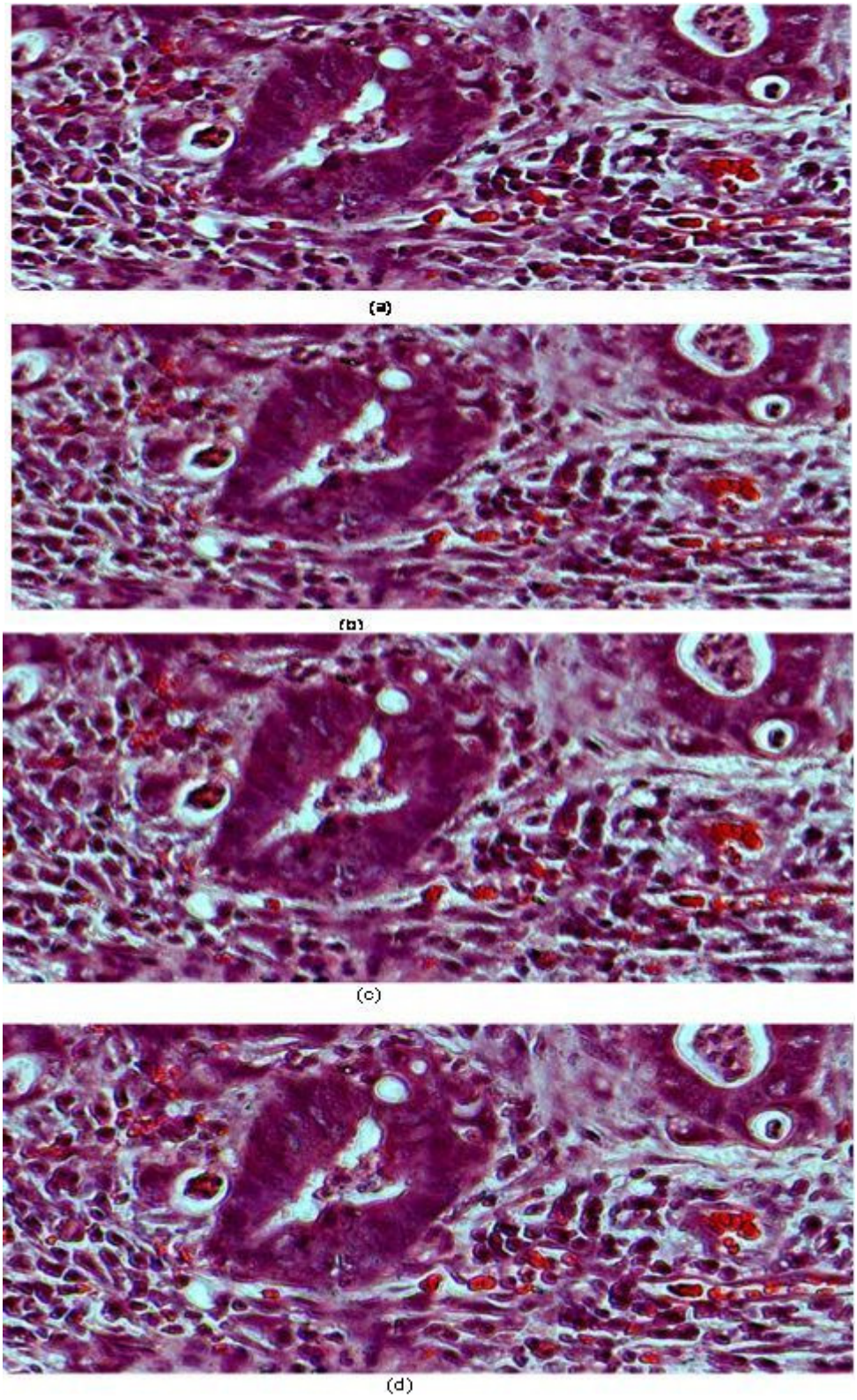

Figure 15. Examples of images used for this study, generated by the digital image fusion methods described in the text (a) is the original image of the specimen, selected as the most in-focus image from a stack of C_n. (b) is the result of a neighborhood-based image fusion, using a 3×3 differential operator. (c) is the result of a neighborhood-based image fusion using a 5×5 differential operator and (d) is the result of a neighborhood-based image fusion, using a 5×5 coefficient of variance operator.

Table 3. Comparison of the previous methods and the composite AF methods.

	Previous method	Method of this study
Size of scan area	10 × 10 mm	
Image size	20000 × 20480 pixels	
Preliminary work	Na	Guide curve
AF mode	Each FOV	Continuous of full trip
Time-consuming		
Build guide curve	0s	62s
Image acquisition (layers)	57s×5	21s×5
Total (s)	285	167

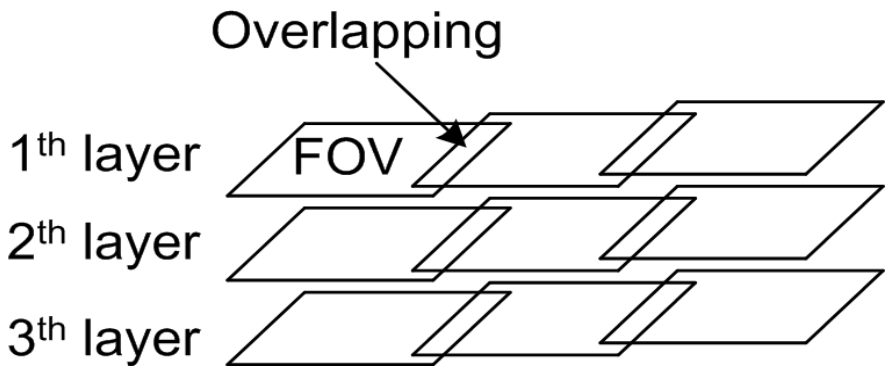

Figure 16. Use of area scan camera for EDOF.

DISCUSSION

The method described combined EDOF with full-trip technology. A line scan camera was used to gather focusing information, before the image was scanned. These two methods were successfully combined, with no increase in processing time. Table 3 shows a comparison between the methods used in this study and other methods that can be used to scan an area of a tissue slide. In previous studies, the use of an area scan camera, for image fusion using EDOF, often lengthened the image acquisition time, as the number of layers to be scanned increased. Each attempt to reach the next FOV required the repetition of AF and multilayer image capture.

Figure 16 shows the use of the area scan camera, for image scan of the tissue slide. The image acquisition, for each adjacent FOV, is not continuous. The area scan camera must complete the multilayer focus for one FOV, before repeating the same process for the next FOV. In this study, the line scan camera captured same-layer images continuously and in focus. To scan images in other layers, it was only necessary to shift the guide curve. This eliminated several steps is used in past procedures. Subsequently, the procedural steps for this study are compared to those for established methods:

Previous method

Step 1: Perform AF, for one FOV.
Step 2: Capture multilayer images, for one FOV.
Step 3: Fuse multilayer images, for one FOV.
Step 4: Move to next FOV and repeat steps 1 to 3

This study

Step 1: Complete the bridging of the guide curve, using an area scan camera.
Step 2: Shift the guide curve, to complete the multilayer image scan, using a line scan camera.
Step 3: Fuse the multilayer images from each full-trip.

Conclusion

This study successfully used an area scan camera to carry out AF at each measurement point. The focus data at each measurement point was used to form a guide curve, which eliminated the problems associated with line scan cameras and AF. As a result, the line scan camera captured tissue images, at constant velocity, while also continuously performing AF, for the full trip. The line scan

camera used EDOF technology to shift the guide curves and capture images in multiple layers. Consequently, images of a slice of a certain thickness were scanned using this composite AF method and the images from multiple layers were rapidly fused, to create a clear image of the tissue slice.

REFERENCES

Dowski ER, Cathey WT (1995). Extended Depth of Field through Wavefront Coding. Appl. Optics, 34: 1859-1866.

Eguíluz C, Viguera E, Millán L, Pérez J (2006). Multitissue array review: A chronological description of tissue array techniques, applications and procedures. Pathol. Res. Pract., 202: 561-568.

Firestone L, Cook K, Gulp K, Talsania N, Preston KJ (1991). Comparison of autofocus methods for automated microscopy. Cytometry, 12: 195-206.

Forster B, Van DVD, Berent J, Sage D, Unser M (2004). Complex Wavelets for Extended Depth of Field: A New Method for the Fusion of Multichannel Microscopy Images. Microscopy Res. Technique, 65: 33-42.

Groen FC, Young IT, Ligthart G (1985). A comparison of different focus functions for use in autofocus algorithms. Cyrometry, 6: 81-91.

Harms H, Aus HM (1984). Comparison of digital focus criteria for a TV microscope system. Cyrometry, 5: 236-243.

He J, Zhou R, Hong Z (2003). Modified fast climbing search auto-focus algorithm with adaptive step size searching technique for digital camera. IEEE Trans. on Consumer Electronics, 49: 257-262.

Kuo WM, Chuang SF, Nian CY, Tarng YS (2008). Precision nano-alignment system using machine vision with motion controlled by piezoelectric motor. Mechatronics, 18: 21-34.

Li H, Manjunath BS, Mitra SK (1994). Multisensor Image Fusion Using the Wavelet Transform. Graphical Models and Image Processing, 57(3): 235-245.

Mea VD, Viel F, Beltrami CA (2005). A pixel-based autofocusing technique for digital histologic and cytologic slides. Computerized Medical Imaging and Graphics, 29: 333-341.

National Instrument Corporation (2007). NI Vision Concepts Manual. National Instrument Corp., Austin, Texas.

National Instruments Corporation (2000). IMAQ Vision Concepts Manual, Texas.

Nian CY, Trang YS (2005). An auto-alignment vision system with three-axis motion control mechanism. Int. Adv. Manuf. Technol., 26: 1121-1131.

Pieper RJ, Korpel A (1983). Image Processing for Extended Depth of Field. Appl. Optics, 22: 1449-1453.

Prabhat P, Ram S, Ward ES, Ober RJ (2006). Simultaneous Imaging of Several Focal Planes in Fluorescence Microscopy for the Study of Cellular Dynamics in 3D. Proceedings of the Society of Photo-Optical Instrumentation Engineers, 6090: 115-121.

Rafael GC, Woods RE (2002). Digital image processing. Prentice Hall Second Edition, pp. 698-705.

Strang G (1999). The discrete cosine transform. SIAM Review, 41: 135-147.

Tympel V (1996). A New High-Level Image Capture System for Conventional Light Microscopy. In Proceedings of the SPIE, 2707: 529-536.

Zhang Z, Blum RS (1999). A Categorization of Multiscale-Decomposition-Based Image Fusion Schemes with a Performance Study for a Digital Camera Application. Proceedings of the IEEE, 87: 1315-1326.